Shap. Mem. Superelasticity (2022) 8:188–199
https://doi.org/10.1007/s40830-022-00383-0

TECHNICAL ARTICLE

Change in the Crystallographic Texture of the Martensitic Phase in Superelastic Ti–Zr–Nb Alloys with Increasing Tensile Strain

Mariia Zaripova[1] · Vladimir Fesenko[1] · Olga Krymskaya[1] · Ilya Kozlov[1] · Roman Svetogorov[2] · Margarita Isaenkova[1]

Received: 3 February 2022 / Revised: 6 July 2022 / Accepted: 5 August 2022 / Published online: 25 August 2022
© ASM International 2022

Abstract Superelastic alloys based on Ti–Zr–Nb are low-modulus biocompatible alloys for medical applications. We analyzed the regularities of the development of martensitic transformations (MT) β (bcc) → α″ (orthorhombic lattice) in Ti–(17–19)Zr–(14–15)Nb (at.%) alloys, where α″-phase arises under the influence of tensile or compressive stress. The crystallographic texture of β-titanium alloys was well studied. However, this is precisely what determines the recoverable strain in the material. Phase analysis using synchrotron radiation showed that the MT begins at 1% deformation, and at 1.5% the martensite lines are clearly distinguishable. The orientational dependences of the formation of domains of the martensite phase were studied using generalized direct pole figures. The main texture components of the cold rolled up to 97% and then recrystallized foils are $\{221\}\langle 114\rangle$ and $\{100\}\langle 011\rangle$. Under tensile deformation up to 1.4%, α″-phase domains with the orientation (100)[001] is formed from β-grains compressed along the normal direction of the foil. With an increase in the degree of deformation to 1.6%, in addition to the main texture component, the second texture component appears. Its orientation depends on the direction of application of the external stress: (001)[110] in tension along the rolling direction and $(\bar{1}05)[501]$ in tension in the transverse direction.

✉ Mariia Zaripova
MMZaripova@mephi.ru

[1] National Research Nuclear University MEPhI (Moscow Engineering Physics Institute), Kashirskoe shosse, 31, Moscow, Russian Federation 115409

[2] National Research Center "Kurchatov Institute", 1, Akademika Kurchatova Pl., Moscow, Russian Federation 123182

Keywords Martensitic transformations · Shape memory alloys · Superelasticity · Crystallographic texture · X-ray diffraction · Synchrotron radiation

Introduction

Superelastic titanium alloys are unique functional materials capable of restoring significant mechanical deformation, several times higher than the values of conventional elastic deformation. This property is useful and necessary for a wide range of biomedical applications [1]. Superelasticity in β-Ti alloys is due to the occurrence of reversible martensitic transformations (MT), which can be caused by tensile or compressive stress, as well as temperature changes.

Currently, TiNi alloys are widely used for medical purposes, since they have excellent mechanical properties and the necessary level of reversible deformation, sufficient to implement the necessary functional properties of structures [2]. For example, a large amount of elastic deformation is of decisive importance in the manufacture of orthodontic arches and intravascular stents [3, 4]. However, as shown in [5–7], Ni has toxic properties, can cause hypersensitivity and allergic reactions. Therefore, it becomes urgent to create new nickel-free medical alloys based on titanium.

β-titanium alloys are a potential substitution for titanium nickelide. It is known [8, 9] that many Ti-Nb alloys show superelastic properties at room temperature. Nowadays, many Ti–Nb-based alloys have been developed, doped with additional elements biocompatible with human organisms: Zr, O, N, Ta, Al, Pt, etc. [10–18]. However, most of these alloys have a small transformation strain compared to TiNi alloys. Among the many alloying

elements, Zr and Ta have received the most attention due to their excellent biocompatibility [10, 19]. As noted in [20], the addition of Zr, partially replacing Nb, is the most effective way to increase reversible deformation while maintaining the transformation temperature. Therefore, in this work, the main attention is paid to Ti–(17–19)Zr–(14–15)Nb (at.%) alloys with similar composition.

The stress-induced MT, that is, arising upon deformation of the β-phase at room temperature [21], includes expansion in one of the $\langle 110\rangle_\beta$ directions and compression in the $\langle 100\rangle_\beta$, and the type of direction depends on the relationship between the crystal orientation and the direction of the applied load. Since the martensite phase in β-titanium alloys is unstable at room temperature (if not fixed by dislocations or precipitates), the reversible phase transformation of martensite into austenite occurs during unloading. The strain associated with the reversible phase transformation results in larger superelastic strain in β alloys [22].

Reversible MT occur in superelastic β-Ti alloys: β (bcc) → α″ (orthorhombic lattice), which is in accordance with the orientation relations [21, 23, 24]:

$$[100]\alpha'' - [100]\beta; [010]\alpha'' - [011]\beta; [001]\alpha'' - [0\bar{1}1]\beta \quad (1)$$

It is also reported [20] that the control of the crystallographic texture is important for achieving a higher value of the recovery strain in the implementation of SE, since the deformation of the transformation from the β-phase to the α″-phase is highly anisotropic. Therefore, in SE alloys, it becomes urgent to create such a texture that will provide an increase in the required functional and performance characteristics [23–26]. In addition, texture optimization can reduce the Young's modulus of biomedical β-titanium alloys to the level of the elastic modulus of bone tissue [13].

There are many studies of the crystallographic texture of Ti alloys with shape memory and superelasticity, most of which are collected in [27]. However, as stated in article [28], the value of reversible deformation is primarily related to the ability of the material to provide consistent alignment of the martensitic twins in a stress field. In other words, the crystallographic texture of the martensite phase determines the recoverable strain in the material. Unfortunately, the results of studies of the texture of martensite induced by stress are extremely few, and they were mainly carried out on TiNi alloys [28, 29]. For example, in [30], the kinetics of MT under uniaxial loading was investigated and the efficiency of X-ray diffractometry for separating peaks of β- and α″-phases was proved; however, studies of the texture of the martensite phase were not carried out.

It should be noted that the uniaxial stress field (for example tension or compression) promotes the growth of some domains of martensite in comparison with others; therefore, it is necessary to consider the texture that forms in the martensite phase.

Thus, the aim of this work is to establish the development of the crystallographic texture of the martensitic phase in superelastic titanium alloys depending on texture of the parent phase with varying orientation and degrees of tensile stresses.

Materials and Methods

Materials Production and Specimen Preparation

Ingots of the studied alloys Ti–(17–19)Zr–(14–16)Nb (at.%) (their compositions are presented in the Table 1) were smelted in an electric arc furnace in an argon atmosphere. After smelting, they were homogenized at 1000 °C for an hour, then heated by induction to 900 °C and forged by compression in two directions perpendicular to the axis of the ingot in order to reduce the grain size. The ingots obtained after forging were rolled to 97% of deformation (the degree of deformation was estimated from the change in the thickness of the ingot), foil thickness is 120 μm. Next, some foils were annealed at 650 °C for 0.5 h (in a flat state) with quenching in water to fix the β-phase and subsequent chemical etching in a mixture of acids (HNO_3:HF:H_2O = 45:10:45). The dimensions of the investigated samples, cut from foils, were 17 × 17 mm. The main directions in the foil as follows: RD—rolling direction, TD and ND—transverse and normal directions, respectively.

Since martensitic transformations occur in the investigated alloys under the action of tensile or compressive stress, in order to study the martensite phase in the obtained samples, it is necessary to create a stressed state, under the action of which the transformations will occur. We deformed the samples by bending and then straightening them. A detailed scheme for preparing samples for X-ray studies is shown in Fig. 1 and consists of 4 stages as follows:

Table 1 Results of elemental analysis of the studied alloys Ti–(17–19)Zr–(14–16)Nb (at.%), carried out on SEM TESCAN LYRA3

Alloy no	Elemental composition (at.%)		
	Ti	Zr	Nb
1 (18–14)	67.6	17.9	14.5
2 (18–15)	66.4	18.4	15.2
3 (18–16)	65.4	18.4	16.2
4 (17–15)	67.4	17.1	15.5
5 (19–15)	65.1	19.3	15.6

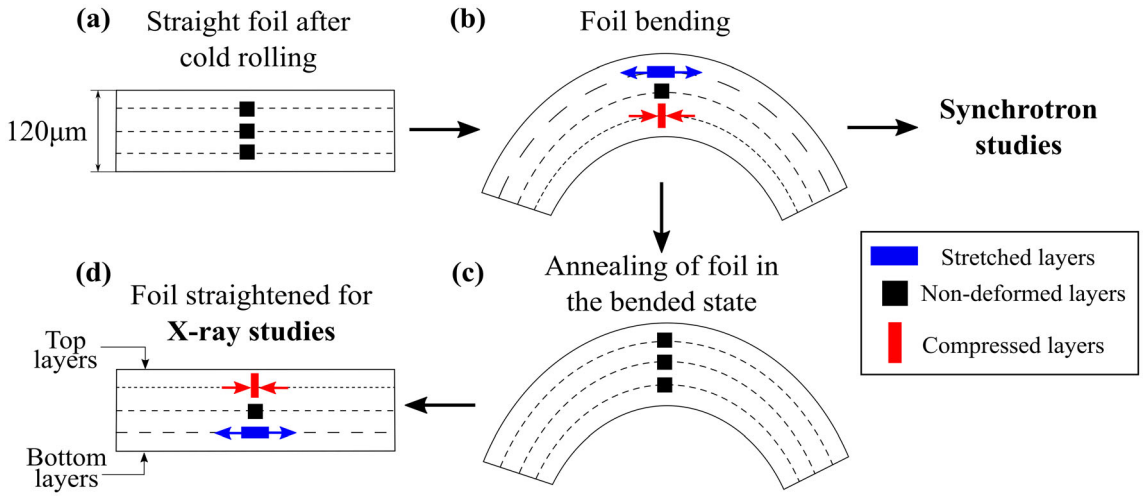

Fig. 1 Sample preparation for synchrotron (**b**) and X-ray (**d**) studies: flat foil after cold rolling (ε = 97%) (**a**) was bended (**b**), placed in a glass tube and annealed in a bended state (650 °C, 0.5 h) (**c**), after that the foil takes the form of a tube, then the foil is straightened (**d**) so that the top layers of foil are compressed and the bottom layers are stretched (Color figure online)

Stage 1.1 Cold rolling, ε = 97% (Fig. 1a).

Stage 1.2 Flat foil (after rolling) was bended and placed in glass tubes of different diameters (to obtain different deformation degrees) (Fig. 1b).

Stage 1.3 Annealing the foil (650 °C for 0.5 h) in a bended state (in a glass tube) to fix the foil in a bended state (Fig. 1c) followed by water quenching. After that, the foil takes the cylindrical form and became the same diameter as a tube.

Stage 1.4 Straightening the foil with a specialized holder made of vanadium (Fig.1d).

Thus, we get the stress state shown in Fig. 1d: the bottom layers (thickness 10–12 μm) of the sample are in tension, the top layers are in compression.

The deformation of the bottom and top layers of foil during bending (and, consequently, during straightening) was evaluated by the equation:

$$\varepsilon = \frac{h}{d+h} \bullet 100\% \quad (2)$$

h is the foil thickness (120 μm), d is the diameter of the tube into which the foil was placed. We used tubes of two diameters: 8.5 mm and 7.4 mm for a subsequent strain of 1.4% and 1.6%, respectively.

It is known that an asymmetry of tensile and compressive deformation during bending (and during straightening) of a bended foil is possible, leading to the fact that its axis lies outside the center of the cross section. However, in this work, this deviation does not play a significant role because we work with a small deformation.

In order to investigate the anisotropy of the phase transformation process, as well as the effect of compressive and tensile stresses on the course of MT, the foils were bended (at the Stage 1.2 of sample preparation, Fig. 1b) around two directions: the RD (bend axis ∥ RD) (Fig. 2a) and the TD (bend axis ∥ TD) (Fig. 2b).

When we bended the sample (at the Stage 1.2) around the RD (Fig. 2a), then in the process of straightening the foil, the bottom layers of foil experienced tension in the TD, and the top layers experienced compression in the TD (the top and bottom layers of the sample when straightened are shown in Fig. 1d). When we bended the samples around the TD (Fig. 2b), after straightening the bottom layers of foil experienced tension along the RD, and the top layers experienced compression along the RD. Thus, we have obtained the first set of samples (for X-rays studies) stretched along the RD or TD.

The penetration depth of X-rays (in the case of the Cu-radiation and titanium alloys) is about 10–12 μm (half-reduction layer of X-ray), therefore, in the process of X-ray measurements, we register reflections only from surface layers. This paper presents the results for specimens taken

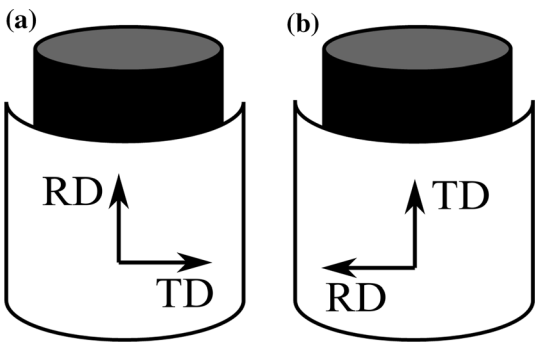

Fig. 2 Schemes of deformation of foils: bending parallel to the initial RD (**a**) and TD (**b**)

from bottom layers (Fig. 1d), i.e. tensile either in the rolling direction or in the transverse direction (depending on the bend pattern shown in Fig. 2). Therefore, in what follows, for simplicity, we will say "stretched sample" instead of "stretched bottom layers of the sample".

Samples for synchrotron studies were prepared according to the following scheme:

Stage 2.1 Cold rolling, ε = 97% (Fig. 1a), up to a thickness of 120 μm.

Stage 2.2 Annealing at 650°C for 0.5 h (in flat state) followed by quenching in water.

Stage 2.3 Bending the foil around brass rods (as it shown in the Figs. 1b and 2a) with diameters of 10 and 8 mm and fixed with a nichrome wire. In this case, the foil was deformed (top layers stretched, bottom layers compressed) up to ε = 1% in the case of a rod diameter of 10 mm and ε = 1.5%—with a diameter of 8 mm (deformation was also estimated by Eq. 2). The foils were bended so that 2–3 mm of the foil rose above the rod.

As a result, we received the second set of samples (for synchrotron studies) of different alloys (Table 1), bended by 1 and 1.5% deformation. The scheme for synchrotron studies of these samples is described below and presented in Fig. 3.

Research Methods

The elemental analysis of the ingots of the Ti–(17–19)Zr–(14–16)Nb (at.%) alloys carried out on SEM TESCAN LYRA3.

The phase composition of the studied samples (flat annealed, as well as bended samples up to 1% and 1.5% deformation) was refined by the Rietveld method using an experimental station for X-ray structural analysis of the Kurchatov synchrotron radiation source [31] with monochromatic radiation with a wavelength of λ = 0.74 Å. The measurements were carried out in the Debye–Scherrer geometry (in transmission) (Fig. 3). The diffraction patterns were recorded with a Rayonix SX165 detector located at 80 mm. The exposure time was from 10 to 120 s (this article presents the spectra measured with an exposure of 60 s). The obtained two-dimensional Debyegrams were integrated to the one-dimensional form I(2θ) using the Dionis program [32].

Also, the diffraction spectra of the studied samples were taken on X-ray diffractometer DRON-3 M with filtered Cu Kα radiation. It should be noted that as a result (after the Stage 1.4, Chapter 2.1) the samples for X-ray studies were in a straightened (flat) state, which made it possible to perform measurements while realizing all the requirements of X-ray diffractometry (subject to the Bragg–Brentano focusing conditions).

A positive factor in measurements at the synchrotron is the use of a two-coordinate detector, which makes it possible to register a complete Debye ring, the intensity along which is summed up. Thus, the intensity of reflections and the sensitivity of detecting additional phases increase, i.e. the preferred orientation does not affect the diffraction spectrum. Moreover, the high intensity of synchrotron radiation (compared to X-ray) makes it possible to understand at what stage of deformation the martensite transformation begins and at what deformation the lines of the martensite phase will be clearly distinguishable.

However, in the case of using a synchrotron radiation source, it is possible to significantly increase the volume of

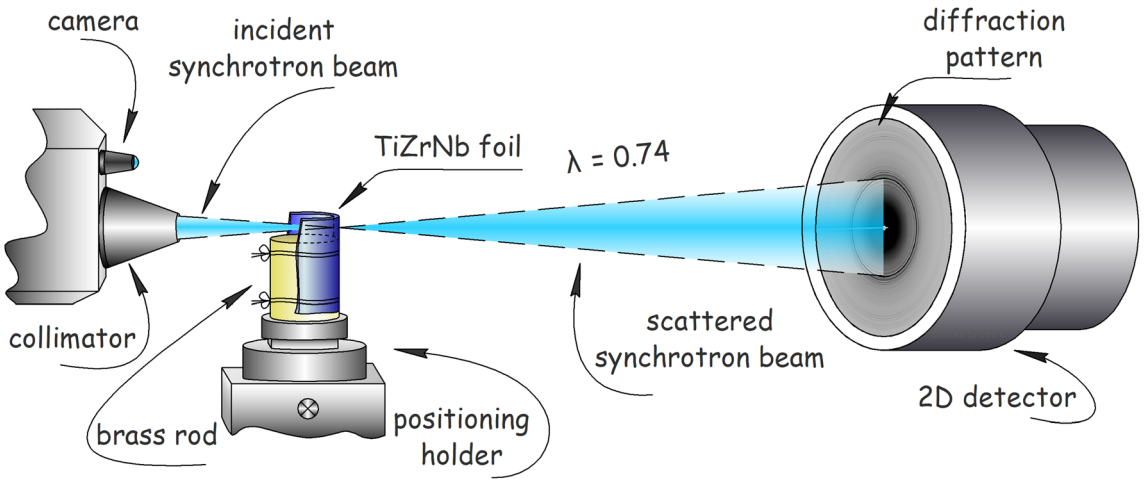

Fig. 3 Schematic view of the X-ray structural analysis beamline measuring zone using synchrotron radiation (Color figure online)

the investigated material (measurements "in transmission", i.e. the thickness of the sample multiplied by the cross-sectional area of the beam). Unfortunately, with such a measurement, all the layers of the sample (both stretched and compressed) are found in the bulk of the material; therefore, MT are fixed that occur on different sides of the bended foil and are caused by both tensile and compressive stresses (Fig. 1b).

Texture analysis of samples after cold rolling, as well as after annealing in the flat state, was carried out with help of DRON-3 X-ray diffractometer with filtered Cu Kα radiation. The crystallographic texture stretched samples was analyzed by generalized direct pole figures (GDPF) [33–36]. The survey of GDPF was carried out on a Bruker D8 Discover diffractometer using copper radiation. Measurements of the studied samples on both diffractometers is carried out under the conditions of Bragg–Brentano focusing, as mentioned before. The results were processed using standard programs DIFFRAC.Topas, DIFFRAC.FileExchange, as well as programs developed in the laboratory of X-ray texture analysis of the National Research Nuclear University MEPhI [33].

Usually, texture measurements incomplete direct pole figures (DPF) consists in measuring the integrated intensity $I(\psi,\varphi)$ of a certain X-ray reflection (hkl) with successive removal of all possible orientations to the reflective position of the grains by means of discrete rotations of the sample under study around two axes by angles $\Delta\psi$ and $\Delta\varphi$. GDPF give a complete description of the substructural heterogeneity of the material depending on its texture, since in the course of such a survey, in addition to the integral intensity of X-ray reflection, its angular position $2\theta_{hkl}$ and physical broadening $b_{1/2}(hkl)$ are recorded. The obtained parameters of X-ray reflections can be easily recalculated into the structural characteristics of grains of different orientations, as shown in [34–37]. For example, the angular position of the X-ray reflection according to the Wolfe-Bragg formula can be converted into the interplanar distance, averaged over the entire GDPF, and then the relative change in the interplanar distance can be calculated for grains of different orientations, or the so-called elastic deformation of the lattice Δd/d, where d is the average value of the interplanar spaces calculated from the GDPF.

When using X-ray diffractometric analysis of a two-phase textured material, traces of a product phase can be unambiguously identified only in the case of a large amount of it or in the case of a favorable orientation of the reflecting planes. When studying the kinetics of MT in a material, one should consider the heterogeneity of the structure of the initial material [36–39] or the inhomogeneity of the distribution of microstresses in grains of different orientations [40, 41].

To estimate the macrostresses arising due to tension or compression, we used the $sin^2\psi$ method, which consists in recording X-ray reflection at different positions of the sample relative to the initial and reflected beams, which differ in the angle of rotation of the sample relative to the goniometer axis [41].

The orientation of the martensite domains causes a redistribution of the line intensities within the spectrum, which prevents the direct identification of the martensite phase. To identify this phase formed under tensile load, it is necessary to use the method described above for capturing generalized pole figures.

As it mentioned before, X-rays capture only surface layers that are in a compressed or stretched state (Fig. 1d). Therefore, the construction of GDPF makes it possible to separate the orientation of grains formed under uniaxial loading (tension or compression).

Results and Discussion

Phase Analysis

Figure 4 shows the X-ray and synchrotron spectra of some of the studied foils.

An analysis of the spectra obtained using synchrotron radiation (with a monochromatic wavelength $\lambda = 0.74$ Å and converted to a copper $K_{\alpha 1}$ radiation wavelength of 1.5406 Å) indicates that in the initial state the studied foils are also in a single-phase state (β-phase). At 1% deformation, lines of the martensitic α''-phase appear in the spectra. The amount of the phase increases significantly with an increase in the degree of foil deformation from 1 to 1.5%. In this case, due to the summation over the Debye rings, all possible reflections for the α''-phase are observed. Note that the intensity of the β-phase lines in the synchrotron radiation spectrum is 20–50 times higher compared to the X-ray reflections of the same lines (in Table 2, compare green and blue lines on Fig. 4).

In the stretched foils, lines of the martensitic phase appear, and it is possible to fix mainly only the line (200) α''-phase due to the preferential orientation of the corresponding planes parallel to the investigated cylindrical surface. However, when measuring the direct pole figures (DPFs) at certain angles of inclination and rotation, other lines of the martensitic phase are visible ((110), (112), (021) for example). In the X-ray diffraction spectrum (Fig. 4, green line) at the Bragg angle $2\theta = 44°$, a line of nichrome wire is also recorded, with the help of which the samples are held on the brass rods.

The processing of the results obtained using the Rietveld method makes it possible to obtain the characteristic

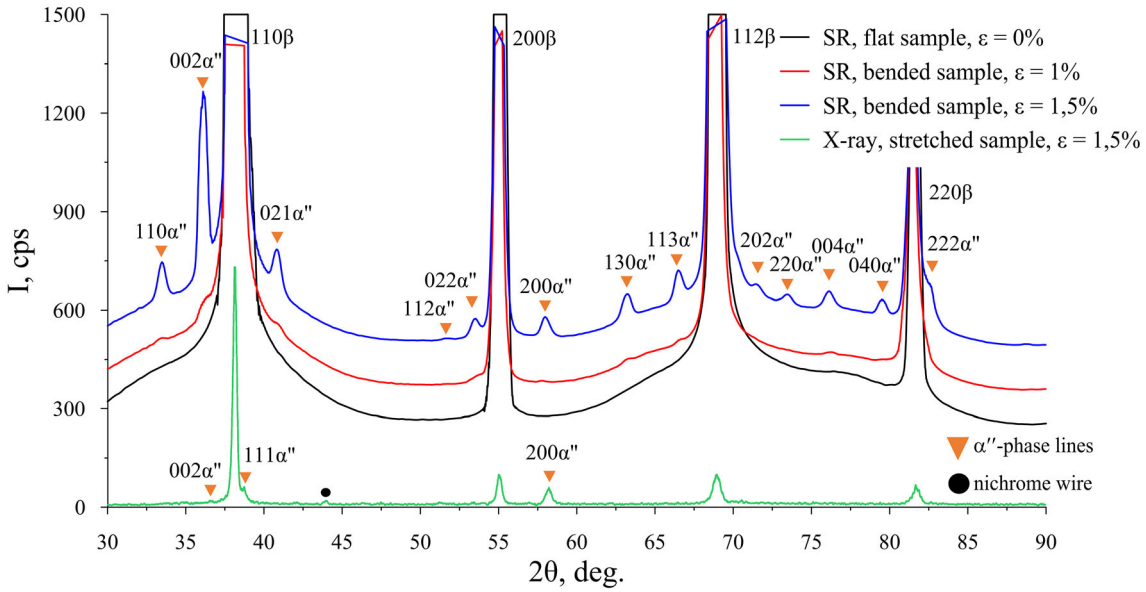

Fig. 4 X-ray (Cu K_α) (green) and synchrotron radiation (SR) diffraction spectra recalculated to the wavelength of Cu $K_{\alpha 1}$ radiation (1.5406 Å): flat sample (black) after annealing at 650 °C, 0.5 h, deformation by bending $\varepsilon = 1\%$ (stretching of the top layers, compression of the bottom layers up to 1%) (red), deformation by bending $\varepsilon = .5\%$ (blue). All results are presented for the Ti–18Zr–15Nb (at.%) alloy (Color figure online)

Table 2 Ratio of line intensities obtained on Ti–18Zr–15Nb (at.%) alloy samples bended up to $\varepsilon = 1.5\%$

Line	$I_{X\text{-ray}}$ (cps)	$I_{Synchrotron}$ (cps)	$I_{Synchrotron}/I_{X\text{-ray}}$ (cps)
(110)	716	16,356	23
(200)	98	2310	24
(112)	97	3830	40
(220)	56	1083	19
(222)	17	850	50

parameters of the structural-phase state of pre-annealed foils of five Ti–Zr–Nb alloys at various deformation degrees. For five Ti–Zr–Nb alloys, Table 3 lists the lattice parameters and the full widths on half maximum (FWHMs) of the X-ray reflections of both phases ($(200)_\beta$ and $(200)_{\alpha''}$), calculated from the diffraction spectra, and also indicates the phase composition calculated from the synchrotron data.

From the presented spectra (Fig. 4) in Ti–18Zr–15Nb (at.%) alloy MT begins at deformation $\varepsilon = 1\%$. In this alloy, even at 1% deformation, 10 wt% of the martensite phase is recorded. At a deformation of 1.5%, the lines of the martensite phase are clearly distinguishable. Therefore, we will consider the results of texture analysis using the example of alloy Ti–18Zr–15Nb (at.%). We have measured the GDPF of samples stretched by more than 1%, namely by 1.4% and 1.6%, i.e. when the lines of the martensitic phase are reliably fixed.

Macrostress Analysis

According to the $sin^2\psi$-method, we measured the macrostresses that occur during the deformation scheme shown in Fig. 1d ($\varepsilon = 1.6\%$). Stresses are measured from both

Table 3 Lattice parameters of the β-phase, phase composition and full width on half-maximum (FWHM) of X-ray lines of both phases ($(200)_\beta$ and $(200)_{\alpha''}$) of samples of five Ti–Zr–Nb alloys at different degrees of deformation

Alloy (at.%)	a (Å)	Amount of α″-phase (wt%)		FWHM ($b_{1/2}$) (°)				
				$\varepsilon = 0\%$	$\varepsilon = 1\%$		$\varepsilon = 1.5\%$	
		$\varepsilon = 1\%$	$\varepsilon = 1.5\%$	$(200)_\beta$	$(200)_\beta$	$(200)_{\alpha''}$	$(200)_\beta$	$(200)_{\alpha''}$
Ti–17Zr–15Nb	3.3422	8.5	10.4	0.13	0.33	0.55	0.46	0.30
Ti–18Zr–14Nb	3.3491	9.6	18.7	0.15	0.29	0.34	0.32	0.38
Ti–18Zr–15Nb	3.3405	10.5	17.3	0.12	0.27	0.22	0.29	0.46
Ti–18Zr–16Nb	3.3542	7.5	12.1	0.13	0.24	0.32	0.30	0.39
Ti–19Zr–15Nb	3.3442	7.2	12.5	0.15	0.24	0.29	0.29	0.38

sides of the sample: from the top and bottom layers. On the bottom side, a positive value of 509 MPa was obtained, therefore, tensile stresses really act, therefore, the sample is in a stretched state. To be precise, not the entire sample is stretched, but only its bottom layers (as shown in Fig. 1d). However, earlier, for simplicity of description, we agreed to consider this a stretched sample, which turned out to be a true statement. On the top side of the sample, the stresses were − 427 MPa, i.e. it is a compression state. Therefore, the result obtained coincides with our reasoning about the deformation scheme implemented in our work presented in Chapter 2.1.

Texture Analysis

Texture analysis was carried out on flat samples: after cold rolling, after annealing and after stretching around RD or TD. The analysis of the obtained incomplete DPF showed that in the foil rolled up to $\varepsilon = 97\%$ from alloy Ti–18Zr–15Nb (at.%), the weak texture $\{112\}\langle 110\rangle$ is formed (Fig. 5a, b). As a result of annealing this foil at a temperature of 650 °C for 0.5 h, the texture component $\{221\}\langle 114\rangle$ is sharpened (Fig. 5c, d). The change in texture during recrystallization is clearly seen in the diagrams of the distribution of the difference in pole densities for annealed flat and deformed (after cold rolling up to 97%) samples (Fig. 6a, b). The diagram shows the orientation of the grains grown, as a result, of the recrystallization of the sample (shown in red on the stereographic projection).

The texture of the stretched samples (by 1.4% along the TD or RD) is similar to the texture of flat samples, but the texture maxima $\{221\}\langle 114\rangle$ are blurred in the direction of the texture component $\{100\}\langle 011\rangle$ (Fig. 5e–h). That is, the process of increasing the pole density in the vicinity of the ND continues on the DPF{100}. This process is clearly visible on the inverse pole figures (IPFs) for ND and RD (Fig. 7), which were reconstructed from the DPFs (using the calculation of the orientation distribution function) in the MTEX program [42].

Figure 8 shows the GDPFs of the β and α''-phases of the foils of Ti–18Zr–15Nb (at.%) alloy stretched along TD (a) and along RD (b). As we can see, during deformation according to the scheme shown in Fig. 2a, when the foil bending axis is parallel to the RD, then along the TD the bottom foil layers (Fig. 1d) experiences tension (Fig. 8a, red areas on GDPF $\Delta d/d$), and along the RD—compression. Similarly, in the case where the bend axis ∥ TD (Fig. 2b): the bottom foil layers are stretched from along the RD (Fig. 8b, red areas on GDPF $\Delta d/d$), and they are compressed along the TD. Moreover, all the grains oriented along the diameter ND-RD are in a compressed state, as evidenced by the blue areas on the GDPF $\Delta d/d$.

If we take into account that the maximum compression during MT occurs along the $\langle 100\rangle_\beta$ direction [19], then in these grains that we should expect the appearance of domains of the martensite phase, in which the $\langle 100\rangle_\beta$ axes will also be oriented along the ND-RD diameter. Similar reasoning can be carried out for samples in which grains with the $\langle 100\rangle_\beta$ orientation along the ND-TD diameter are compressed when the foil are stretched along the initial TD.

It is in the grains of the β-phase with the orientation $\langle 100\rangle$ near the ND that the appearance of domains of a new martensite phase is observed. This is confirmed by the

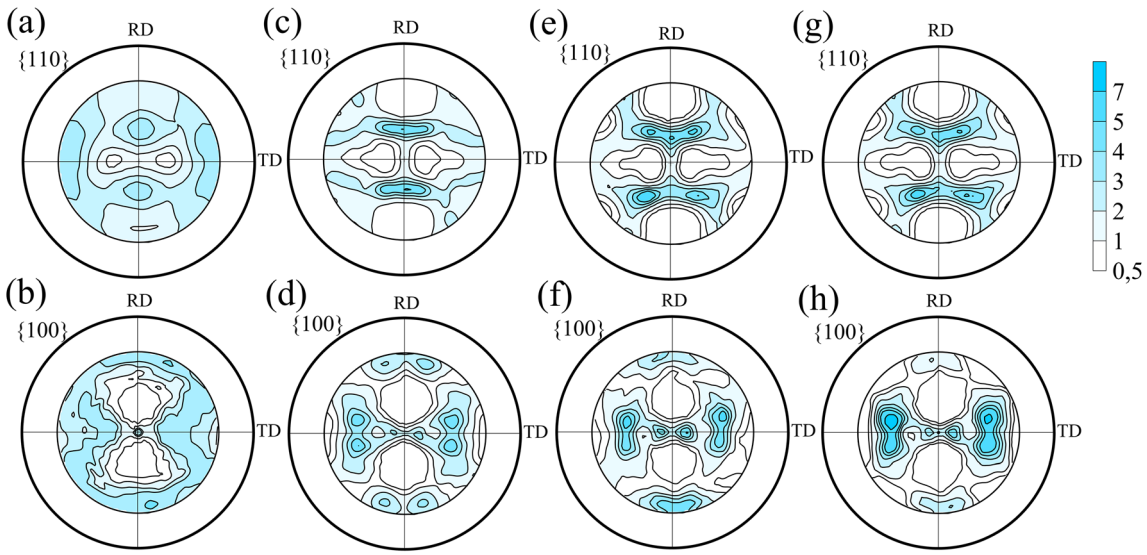

Fig. 5 DPFs{110} and {100} of Ti–18Zr–15Nb (at.%) alloy foils in different states: cold rolled (**a**, **b**), annealed at 650 °C for 0.5 h in the flat state (**c**, **d**), stretched by 1.4% along the TD (**e**, **f**) and stretched by 1.4% along the RD (**g**, **h**) (Color figure online)

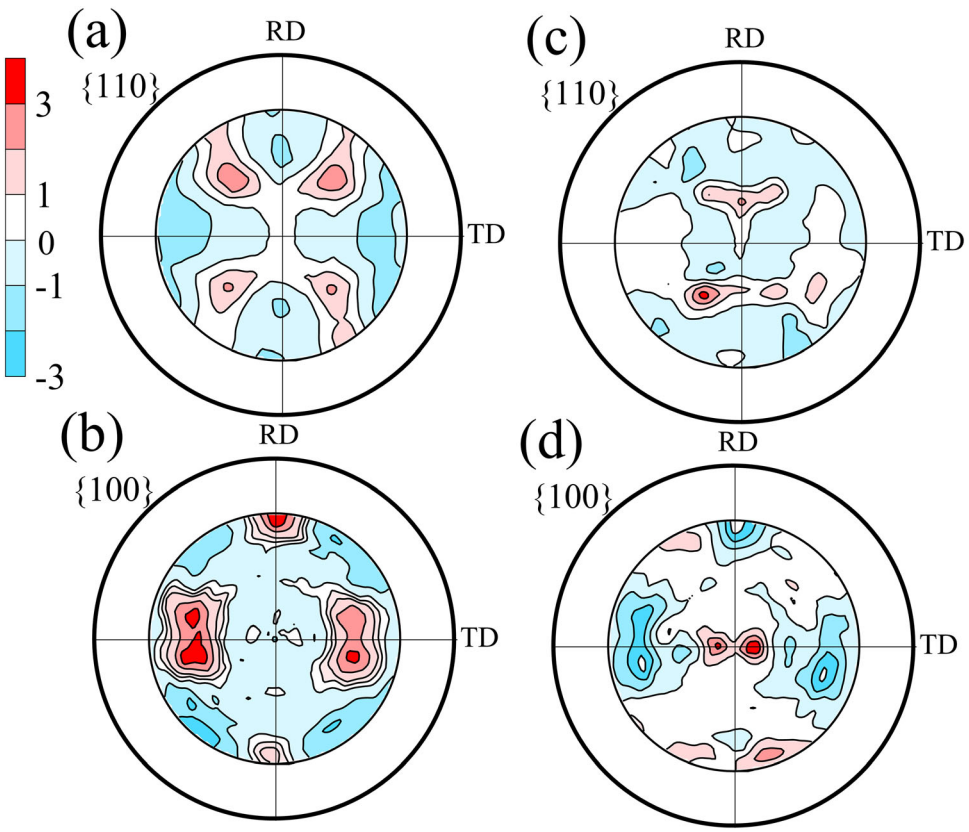

Fig. 6 Distribution diagrams of the difference of the pole densities of annealed and cold-rolled samples (**a**, **b**), as well as sample stretched along the RD (ε = 1.4%) and sample annealed in a flat state (**c**, **d**) (Color figure online)

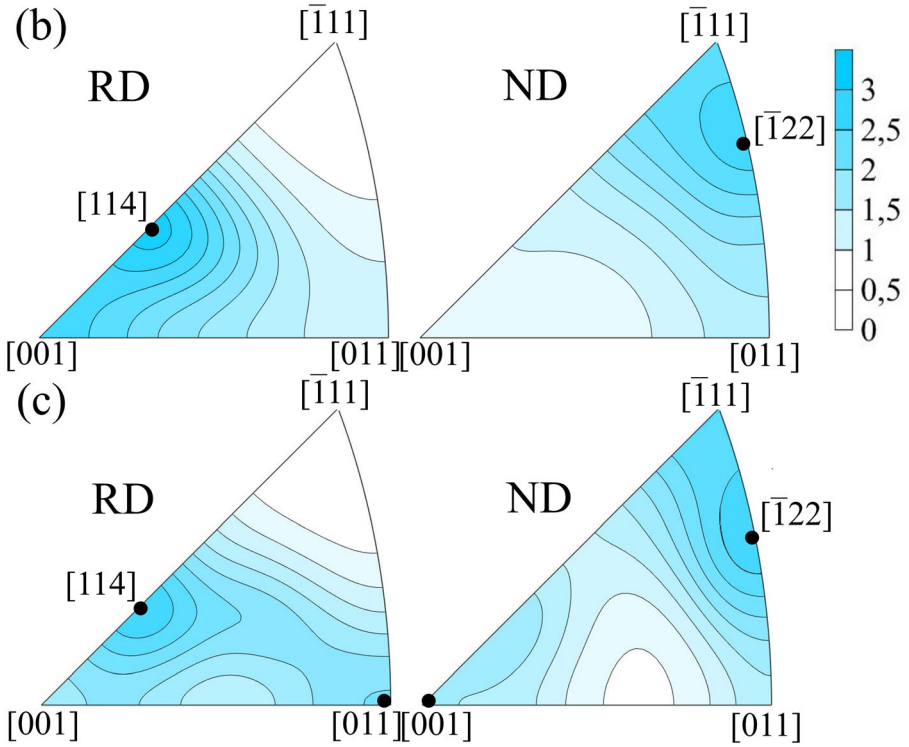

Fig. 7 IPFs for RD and ND of Ti–18Zr–15Nb (at.%) alloy foils in different states: annealed at 650 °C for 0.5 h in the flat state (**a**), stretched by 1.4% along the RD (**b**) (Color figure online)

distribution diagrams of the difference of the pole densities of sample stretched along the RD and sample annealed in a flat state (Fig. 6 c, d) show which grains were formed, as a result, of MTs occurring during tension. Red areas in

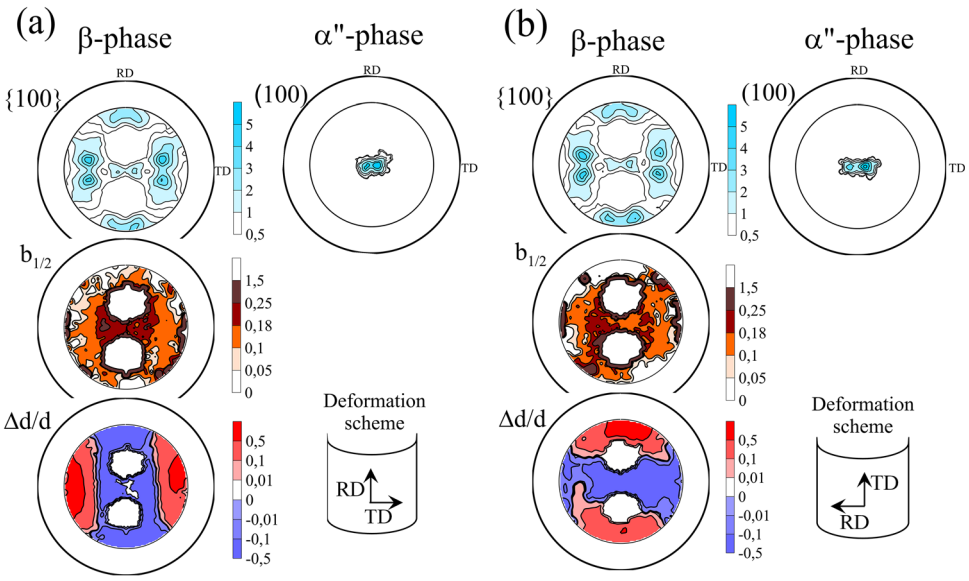

Fig. 8 GDPFs {100} of the Ti–18Zr–15Nb (at.%) alloy foils stretched along the TD (**a**) и RD (**b**) up to 1.4%. For clarity, the deformation scheme is also shown here (Color figure online)

Fig. 6d indicate which orientations are formed during stretching.

As a result of the phase transformation the physical broadening of the line sharply increases (Fig. 8, GDPF $b_{1/2}$ for β-phase). This broadening of the $(200)_\beta$ line was also recorded when analyzing the diffraction spectrum (in Table 3, lines $(200)_\beta$). The broadening of the X-ray line indicates the distortion of the crystal structure associated with the appearance of a martensite phase in them. In such grains, which are characterized by a high value of $b_{1/2}$ (Table 3), the domains of the martensitic phase are located.

Figure 8 shows that at deformation $\varepsilon = 1.4\%$ in the martensitic phase, a one-component texture (100)[001] is formed, where the (100) plane is located almost parallel to the foil rolling plane. A slight misorientation of texture maxima in the transverse direction is obviously associated with the bifurcation of the central texture maximum of the β-phase at GDPF {100} (Fig. 8a) and the observance of the orientation relation: $[100]\beta - [100]\alpha''$.

An increase in the volume fraction of the α''-phase with deformation up to 1.6% made it possible to construct 6 DPFs, with the help of which it is possible to describe the complete orientation of the martensite phase (Fig. 9). The texture components were determined from the full DPFs reconstructed from these 6 DPFs ((200), (112), (110), (111), (021), (011)) using the MTEX program (with setting the orthorhombic geometry) [42].

Deformations of the orthorhombic lattice of martensite along the three main crystal axes can be calculated using the lattice parameters of the parent β-phase (Table 3) and martensitic α''-phase as follows [19]:

$$\eta_1 = \frac{a' - a}{a}, \eta_2 = \frac{b' - \sqrt{2}a}{\sqrt{2}a}, \eta_3 = \frac{c' - \sqrt{2}a}{\sqrt{2}a} \quad (3)$$

The lattice parameters of martensite were refined using the Rietveld method, and the following values were obtained for the Ti–18Zr–15 Nb (at.%) alloy: a = 33,405 Å, a' = 30,427 Å, b' = 47,047 Å, c' = 49,805 Å.

It turns out that during the occurrence of MT, the initial crystal structure undergoes compression in the a' direction by 8.9%, along b'—by 0.4%, while tension by 5.4% occurs along c'. This explains that, at low deformation, MTs are activated in β-grains, which are in a compressed state (Fig. 8a, blue regions of the GDPF $\Delta d/d$). In this case, parallel to the {100} planes of the β-phase, the (100) planes of the α''-phase are oriented, which are most subject to compression along the a' [100] direction (Table 4). Consequently, the MTs take place in a substance with a texture close to $\{100\}\langle 011\rangle$.

An increase of the deformation degree from 1.4 to 1.6% leads to the formation of an additional textural component of the martensite phase. We calculated the deformations of the martensite lattice along the directions for which the DPFs were measured (by changing the lattice parameters during the phase transformation) (Table 4). It was found that during compression, the texture components of the α''-phase are formed in compressed regions (Fig. 9, blue regions of the GDPF Δd/d), and during tension, in stretched ones (Fig. 9, red regions of the GDPF $\Delta d/d$). Moreover, the intensity of the pole density maxima correlates with the amount of strain in each of the directions.

It has been established that if axes of a certain type are compressed during MT, it is formed in compressed regions. For example, during transformations, the normal [100] is undergone compression, as well as [112] (Table 4), and we observe texture maxima on the DPFs (100) and (112) in the

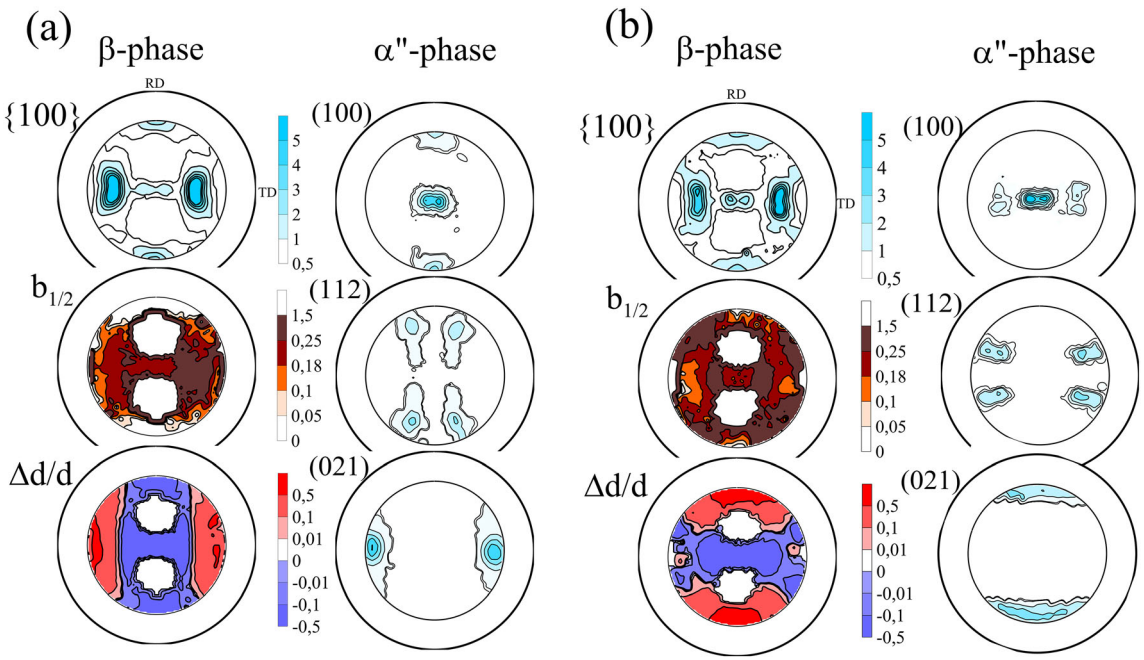

Fig. 9 GDPFs for β- and α''-phases of foil made of Ti–18Zr–15Nb (at.%) alloy, stretched along the TD (**a**) and along RD (**b**) up to 1.6% (Color figure online)

Table 4 Deformations of the orthorhombic lattice of martensite in of foil made of Ti–18Zr–15Nb (at.%) alloy along different directions

Line of α''-phase	Transformation strain (%)	Type of deformation	Pole density (max)
(100)	− 8.9	Compression	4.4
(112)	− 1.5	Compression	2.4
(110)	− 2.9	Compression	3.0
(111)	− 0.3	Compression	1.6
(021)	0.9	Tension	1.4
(011)	2.6	Tension	2.2

compressed areas (Fig. 9, blue areas on the GDPF $\Delta d/d$, DPFs (100) and (112) for the α''-phase), as in tension along the TD (Fig. 9a) so along the RD (Fig. 9b). Similarly, normal [021] is undergone tension during transformations, so we see these reflections in stretched areas (Fig. 9, red areas on GDPF $\Delta d/d$, DPFs (021) for α''-phase).

Thus, at a deformation of 1.6%, a two-component texture is formed. When the sample is stretched along the TD, martensite with the (100)[001] orientation are formed, along with which a second component with the orientation $(\bar{1}05)[501]$ appears (Fig. 10a). When the sample is stretched along the RD, martensite with the (100)[010] orientation is formed and a second component with the orientation (001)[110] appears (Fig. 10b). The IPFs for RD and ND are built using the reconstructed orientation distribution function (in the MTEX program) for 6 DPFs obtained as a result of measuring GDPFs.

Note that MTs in both cases (i.e., in grains of different texture components) occur in the most perfect grains of the β-phase, formed as a result of annealing at a temperature of 650 °C for 0.5 h and corresponding to the orientation of the red regions in the difference diagram (Fig. 6d).

Conclusions

1. The use of synchrotron radiation for the study of martensitic transformations in alloys Ti–(17–19)Zr–(14–16)Nb (at.%) made it possible to reveal from 7 to 10 wt% of the martensite phase at the degree of foil deformation by only 1%. Moreover, clarified that martensitic transformations begins at 1% of deformation, and at 1.5% the martensite lines are clearly distinguishable.
2. It is shown that a weak $\{112\}\langle 110\rangle$ texture is formed in a foil rolled up to 97% from alloy Ti–18Zr–15Nb (at.%). As a result of annealing this foil at a temperature of 650 °C for 0.5 h, the texture component $\{221\}\langle 114\rangle$ becomes sharper. The texture of the stretched samples (by 1.4% along the TD or RD) is

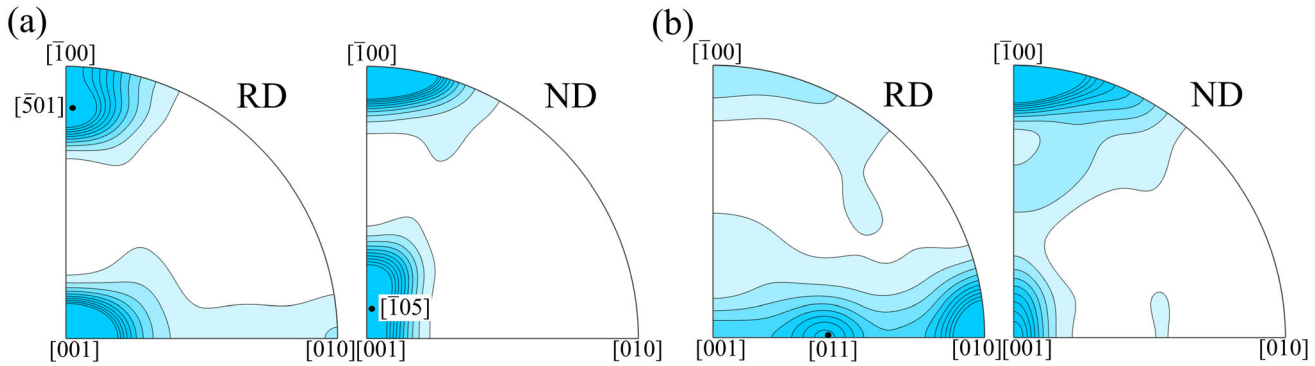

Fig. 10 IPFs for α″-phase of surface layers of sample, stretched along the TD (**a**) and along the RD (**b**) up to 1.6% (Color figure online)

similar to the texture of annealed samples, but the texture maxima {221}⟨114⟩ are blurred in the direction of the texture component {100}⟨011⟩.

3. Using the method of generalized direct pole figures, the sequence of appearance of grains of the martensitic phase of different orientations was established with an increase in the degree of deformation (from 1.4 to 1.6%). It was found, that martensitic transformations begin in recrystallized grains of the initial β-phase, which are in a compressed state during deformation. Martensite transformations begin in compressed (along the normal direction) grains of the β-phase with an orientation close to {100}⟨011⟩, and a martensite phase with the (100)[001] orientation is formed. With an increase in the degree of deformation to 1.6%, in addition to the main texture component, the second texture component appears. Its orientation depends on the direction of application of the stress: (001)[110] in tension along the rolling direction and ($\bar{1}$05)[501] in tension in the transverse direction.
4. Grains of the martensitic phase grow in perfect grains of the β-phase, leading to their significant fragmentation, as evidenced by a twofold increase in the half-width of X-ray reflections of the β-phase.

Acknowledgements The work was carried out with the financial support of the Russian Federation represented by the Ministry of Science and Higher Education of the Russian Federation (Agreement No. 075-15-2021-1352).

Data Availability The data required to reproduce these findings are available to download from [43].

References

1. Ramezannejad A, Xu W, Xiao WL, Fox K, Liang D, Qian M (2019) New insights into nickel-free superelastic titanium alloys for biomedical applications. Curr Opin Solid State Mater Sci 23(6):100783. https://doi.org/10.1016/J.COSSMS.2019.100783
2. Miyazaki S, Miyazaki S (2017) My experience with Ti–Ni-based and Ti-based shape memory alloys. Shape Mem Superelast 3(4):279–314. https://doi.org/10.1007/s40830-017-0122-3
3. Yoneyama T, Miyazaki S (2009) Shape memory alloys for biomedical applications. Woodhead Publishing, England
4. Nuss S, US Patent no. 7.468.045 (2008)
5. Nordberg GF, Gerhardsson L, Broberg K, Mumtaz M, Ruiz P, Fowler BA (2007) Interactions in metal toxicology. Handb Toxicol Met, pp 117–145. https://doi.org/10.1016/B978-012369413-3/50062-8
6. Biocompatibility and tissue reaction to biomaterials. Craig's Restor Dent Mater, pp 109–133 (2012) https://doi.org/10.1016/B978-0-323-08108-5.10006-4
7. Köster R, Vieluf D, Kiehn M, Sommerauer M, Kahler J, Baldus S, Meinertz T, Hamm CW (2000) Nickel and molybdenum contact allergies in patients with coronary in-stent restenosis. Lancet 356(9245):1895–1897. https://doi.org/10.1016/S0140-6736(00)03262-1
8. Kim HY, Hashimoto S, Il KJ, Hosoda H, Miyazaki S (2004) Mechanical properties and shape memory behavior of Ti-Nb alloys. Mater Trans 45(7):2443–2448. https://doi.org/10.2320/matertrans.45.2443
9. Kim HY, Miyazaki S (2016) Several issues in the development of Ti–Nb-based shape memory alloys. Shape Mem Superelast 2(4):380–390. https://doi.org/10.1007/s40830-016-0087-7
10. Bedi RS, Beving DE, Zanello LP, Yan Y (2009) Biocompatibility of corrosion-resistant zeolite coatings for titanium alloy biomedical implants. Acta Biomater 5(8):3265–3271. https://doi.org/10.1016/j.actbio.2009.04.019
11. Kim H-S, Kim W-Y, Lim S-H (2006) Microstructure and elastic modulus of Ti-Nb-Si ternary alloys for biomedical applications. Scr Mater 54(5):887–891. https://doi.org/10.1016/j.scriptamat.2005.11.001
12. Hao YL, Zhang ZB, Li SJ, Yang R (2012) Microstructure and mechanical behavior of a Ti-24Nb-4Zr-8Sn alloy processed by warm swaging and warm rolling. Acta Mater 60(5):2169–2177. https://doi.org/10.1016/j.actamat.2012.01.003
13. Kim HY, Sasaki T, Okutsu K, Kim JI, Inamura T, Hosoda H, Miyazaki S (2006) Texture and shape memory behavior of Ti-22Nb-6Ta alloy. Acta Mater 54(2):423–433. https://doi.org/10.1016/j.actamat.2005.09.014
14. Sun F, Nowak S, Gloriant T, Laheurte P, Eberhardt A, Prima F (2010) Influence of a short thermal treatment on the superelastic properties of a titanium-based alloy. Scr Mater 63(11):1053–1056. https://doi.org/10.1016/j.scriptamat.2010.07.042
15. Zhang J, Sun F, Hao Y, Gozdecki N, Lebrun E, Vermaut P, Portier R, Gloriant T, Laheurte P, Prima F (2013) Influence of equiatomic Zr/Nb substitution on superelastic behavior of Ti-Nb-

Zr alloy. Mater Sci Eng A 563:78–85. https://doi.org/10.1016/j.msea.2012.11.045
16. Miyazaki S, Kim HY, Hosoda H (2006) Development and characterization of Ni-free Ti-base shape memory and superelastic alloys. Mater Sci Eng A 438–440:18–24. https://doi.org/10.1016/j.msea.2006.02.054
17. Ramarolahy A, Castany P, Prima F, Laheurte P, Péron I, Gloriant T (2012) Microstructure and mechanical behavior of superelastic Ti-24Nb-0.5O and Ti-24Nb-0.5N biomedical alloys. J Mech Behav Biomed Mater 9:83–90. https://doi.org/10.1016/j.jmbbm.2012.01.017
18. Fukui Y, Inamura T, Hosoda H, Wakashima K, Miyazaki S (2004) Mechanical properties of a Ti-Nb-Al shape memory alloy. Mater Trans 45(4):1077–1082. https://doi.org/10.2320/matertrans.45.1077
19. Kim HY, Fu J, Tobe H, Il KJ, Miyazaki S (2015) Crystal structure, transformation strain, and superelastic property of Ti–Nb–Zr and Ti–Nb–Ta Alloys. Shape Mem Superelast 1(2):107–116. https://doi.org/10.1007/s40830-015-0022-3
20. Fu J, Yamamoto A, Kim HY, Hosoda H, Miyazaki S (2015) Novel Ti-base superelastic alloys with large recovery strain and excellent biocompatibility. Acta Biomater 17:56–67. https://doi.org/10.1016/J.ACTBIO.2015.02.001
21. Cai S, Daymond MR, Ren Y, Schaffer JE (2013) Evolution of lattice strain and phase transformation of β III Ti alloy during room temperature cyclic tension. Acta Mater 61(18):6830–6842. https://doi.org/10.1016/J.ACTAMAT.2013.07.062
22. Kim HY, Ikehara Y, Kim JI, Hosoda H, Miyazaki S (2006) Martensitic transformation, shape memory effect and superelasticity of Ti-Nb binary alloys. Acta Mater 54(9):2419–2429. https://doi.org/10.1016/j.actamat.2006.01.019
23. Inamura T, Shimizu R, Kim HY, Miyazaki S, Hosoda H (2016) Optimum rolling ratio for obtaining {001}⟨110⟩ recrystallization texture in Ti-Nb-Al biomedical shape memory alloy. Mater Sci Eng C 61(April):499–505. https://doi.org/10.1016/j.msec.2015.12.086
24. Zaripova MM, Isaenkova MG, Perlovich YA, Osintsev AV, Fesenko VA (2019) Influence of crystallographic texture and phase composition on the effect of superelastiñity of foils from alloys based on Ti-Nb. Chelyabinsk Phys Math J. https://doi.org/10.24411/2500-0101-2019-14109
25. Zaripova MM, Isaenkova MG, Fesenko VA, Osintsev AV (2021) The influence of the crystallographic texture and phase composition of Ti-Nb-Zr alloys with shape memory and superelasticity on their functional properties. IOP Conf Ser Mater Sci Eng 1121(1):012032. https://doi.org/10.1088/1757-899x/1121/1/012032
26. Isaenkova MG, Perlovich YA, Fesenko VA, Zaripova MM (2019) Orientation dependence of functional properties of alloys with shape memory effect and superelasticity. Chelyabinsk Phys Math J. https://doi.org/10.24411/2500-0101-2019-14209
27. Kim HY, Miyazaki S (2018) Chapter 4—Thermomechanical treatment and microstructure control. In: Kim HY, Miyazaki S (eds) Ni-free Ti-based shape memory alloys. Butterworth-Heinemann, Oxford, pp 111–145
28. Hasan M, Schmahl WW, Hackl K, Heinen R, Frenzel J, Gollerthan S, Eggeler G, Wagner M, Khalil-Allafi J, Baruj A (2008) Hard X-ray studies of stress-induced phase transformations of superelastic NiTi shape memory alloys under uniaxial load. Mater Sci Eng A 481–482:414–419. https://doi.org/10.1016/J.MSEA.2007.02.156
29. Zheng QS, Liu Y (2002) A Prediction of the detwinning anisotropy in textured NiTi shape memory alloy. Philosoph Mag. https://doi.org/10.1080/01418610208243195
30. Yang Y, Castany P, Cornen M, Prima F, Li SJ, Hao YL, Gloriant T (2015) Characterization of the martensitic transformation in the superelastic Ti-24Nb-4Zr-8Sn alloy by in situ synchrotron X-ray diffraction and dynamic mechanical analysis. Acta Mater 88:25–33. https://doi.org/10.1016/j.actamat.2015.01.039
31. Svetogorov RD, Sulyanov SN (2018) High-resolution powder diffraction at the XSA beamline of the Kurchatov Synchrotron Radiation Source. In: IX National crystal chemical conference, Suzdal, conference proceedings 81.
32. Svetogorov RD, Dionis—diffraction open integration software. Certificate of registration № 2018660965.
33. Perlovich YA, Isaenkova MG (2015) Strukturnaya neodnorodnost' teksturirovannykh metallicheskikh materialov (Structural heterogeneity of textured metal materials). National Research Nuclear University MEPhI, Moscow, 398, In Russ.
34. Perlovich Y, Isaenkova M, Bunge HJ (2001) The fullest description of the structure of textured metal materials with generalized pole figures: the example of rolled Zr alloys. Mater Sci Forum 378–381:180–185. https://doi.org/10.4028/www.scientific.net/MSF.378-381.180
35. Perlovich Y, Isaenkova M (2002) Distribution of c- and a-dislocations in tubes of Zr alloys. Metall Mater Trans A. https://doi.org/10.1007/s11661-002-0156-8
36. Perlovich Yu, Isaenkova M (2005) Distribution of dislocation density in tubes from Zr-based alloys by X-ray data. Solid State Phenom 105:89–94. https://doi.org/10.4028/3-908451-09-4.89
37. Perlovich Yu, Isaenkova M (1997) Features of the phase transformations in sheets, tubes and welding seams of the alloy Zr-2.5%Nb. Text Microstruct 30:55–70. https://doi.org/10.1155/TSM.30.55
38. Fesenko V, Perlovich Y, Isaenkova M (2015) The increased shape memory effect in rolled Ti-48%Ni-2%Fe single crystals. Mater Today Proc 2:S751–S754. https://doi.org/10.1016/J.MATPR.2015.07.391
39. Perlovich Y, Isaenkova M (2011) Non-uniform strain hardening of crystallites within different regions of texture maxima: evidences and mechanisms. Mater Sci Forum 702–703:681–684. https://doi.org/10.4028/www.scientific.net/MSF.702-703.681
40. Perlovich Yu, Isaenkova M, Fesenko V (2008) Three laws of substructure anisotropy of textured metal materials, revealed by X-ray method of generalized pole figures. Mater Proces Text Ceram Trans 200:539–546. https://doi.org/10.1002/9780470444214.ch20
41. Perlovich Y, Isaenkova M, Bunge HJ, Fesenko V (2000) Distribution of residual microstresses in rolled textured metal materials. Mater Sci Forum 347–349:291–296. https://doi.org/10.4028/www.scientific.net/MSF.347-349.291
42. MTEX Toolbox (Electronic resource). https://mtex-toolbox.github.io/index.html. Accessed 19 Nov 2021
43. Zaripova M (2021) Phase and texture analysis data Mendeley Data, V1. https://doi.org/10.17632/2vmgssbt7f.1

Publisher's Note Springer Nature remains neutral with regard to jurisdictional claims in published maps and institutional affiliations.